Oxygen semi-permeation properties of Ba1-xSrxFeO3-δ perovskite membranes

Eva Deronzier, Thierry Chartier, Pierre-Marie Geffroy

▶ **To cite this version:**

Oxygen semi-permeation properties of $Ba_{1-x}Sr_xFeO_{3-\delta}$ perovskite membranes

E. Deronzier[a], T. Chartier [a], P.-M. Geffroy [a]

[a] IRCER, CNRS, Université de Limoges, *CEC, 12 Rue Atlantis, 87068 Limoges, France*

Abstract

This work is focused on the evaluation of oxygen semi-permeation performances of free cobalt perovskite membrane materials, $Ba_{1-x}Sr_xFeO_{3-\delta}$ perovskites. A wide range of Ba and Sr contents were studied. The best performances were obtained for $Ba_{0.9}Sr_{0.1}FeO_{3-\delta}$ perovskite membranes with oxygen fluxes of $4.1 \ 10^{-3}$ $mol.m^{-2}.s^{-1}$ at 850°C. For a better understanding of the rate determining step of oxygen transport through $Ba_{1-x}Sr_xFeO_{3-\delta}$ perovskite membranes, the oxygen diffusion and oxygen desorption coefficients were determined for $Ba_{1-x}Sr_xFeO_{3-\delta}$ perovskite membranes (with x = 0.1, 0.5, and 0.7) by a specific method based on oxygen semi-permeation.

Keywords: oxygen semi-permeation, BSF perovskite membrane, oxygen diffusion, oxygen desorption coefficient.

1. Introduction

For several decades, numerous mixed conductors have been studied as membrane material for oxygen separation or electrodes for SOFC technology. $Ba_{0.5}Sr_{0.5}Co_{0.8}Fe_{0.2}O_{3-\delta}$ (BSCF) perovskite material is one of the most promising materials as the membrane because it has the highest oxygen semi-permeation fluxes. The oxygen semi-permeation phenomenon is due to the mixed conduction (electronic and ionic) in the membrane materials. For instance, Arnold et al. [1] obtained an oxygen flux of approximately 2.7 $ml.cm^{-2}.min^{-1}$ ($2.0 \ 10^{-2}$ $mol.m^{-2}.s^{-1}$) at 875°C through a 1-mm-thick dense membrane under an air/He gradient (feed flow rate 150 ml/min, sweep flow rate 140 ml/min). Buysse et al. [2] found an oxygen flux of 5.3 $ml.cm^{-2}.min^{-1}$ ($3.9 \ 10^{-2}$ $mol.m^{-2}.s^{-1}$) with BSCF hollow fibre at 950°C under an air/Ar (feed flow rate 100 ml/min, sweep flow rate 125 ml/min). The fibre shows an outer diameter of about 3.5mm, and a wall thickness of about 0.4mm. However, this material contains cobalt, which

is harmful and precipitates during sintering of BSCF material at a high temperature. Indeed, the surface of samples sintered at 1150°C shows a secondary phase that is exclusively located at the grain boundary, which constitutes a triple point between two grains and the gas phase [3]. Moreover, this material is not stable at high temperature and under low oxygen partial pressures. Arnold et al. [1] also reported a decomposition of perovskite structure into carbonates and oxides after exposition (some hours) under CO_2.

Thus, numerous works in the literature suggest the improvement of the chemical stability of BSCF perovskite at high temperature by substituting Co with a judicious cation in the B site: $(Ba_{0.5}Sr_{0.5})(Co_{0.8}Fe_{0.2})_{1-z}Zr_zO_{3-\delta}$ [4], $Ba_{0.5}Sr_{0.5}(Co_{0.8}Fe_{0.2})_{1-x}Nb_xO_{3-\delta}$ [5], $Ba_{0.5}Sr_{0.5}Co_{0.8}Fe_{0.2-x}Y_xO_{3-\delta}$ [6, 7], $Ba_{0.5}Sr_{0.5}Co_{0.8-x}W_xFe_{0.2}O_{3-\delta}$ [8], $Ba_{0.5}Sr_{0.5}Co_{0.8-x}Mo_xFe_{0.2}O_{3-\delta}$ [9]. Curiously, only few studies reported the oxygen semi-permeation properties of $Ba_{0.5}Sr_{0.5}FeO_{3-\delta}$ material (denoted BSF55 in this work) or $Ba_{1-x}Sr_xFeO_{3-\delta}$ materials (denoted BSF in this work). Indeed, we suggest that BSF materials present a higher tolerance towards CO_2 compared to BSCF material when the barium rate in BSF materials is lower or equal to 50%. Moreover, Jaiswal et al. [10] have recently shown that 1-mm-thick $Ba_{1-x}Sr_xFeO_{3-\delta}$ (x = 0, 0.04, 0.06, 0.08, 0.1, 1) membranes show high oxygen permeation fluxes under an air/Ar gradient (feed flow rate 400 ml/min, sweep flow rate 40 ml/min).. Teraoka et al. [11] have also reported high oxygen permeation fluxes (3.0 cm^3(STP).cm^{-2}.min^{-1} or 2.2 10^{-2} $mol.m^{-2}.s^{-1}$ at 900°C) though a 1-mm-thick $Ba_{0.3}Sr_{0.7}FeO_{3-\delta}$ membrane under an air/He gradient.

In this context, this work is focused on the study of oxygen permeation properties of $Ba_{1-x}Sr_xFeO_{3-\delta}$ materials with a large ratio of Ba substitution by Sr (with x ranging from 0 to 1). The synthesis and sintering of mixed conductor $Ba_{1-x}Sr_xFeO_{3-\delta}$ (x = 0, 0.1, 0.2, …, 0.9, 1) are presented. The optimization of sintering conditions is essential to obtain dense membranes without cracks with a relative density higher than 95%, required for oxygen semi-permeation measurements. Indeed, in the literature, the sintered membrane samples showed a lower relative density (for instance, 90-94% [5, 12, 13]), which can lead to non-representative high oxygen semi-permeation. Besides, the semi-permeation performances of the membrane can be largely affected by the conditions of semi-permeation measurements [14] (thickness, gradient of oxygen partial pressure, flow of gas in the chamber, etc…).

Then, the interest of study is to measure directly oxygen bulk diffusion and surface exchange coefficients from oxygen permeation fluxes, which can also be compared with data collected in our previous works or in the literature for similar membrane materials. This approach

allows to compare more rigorously the real performances of $Ba_{1-x}Sr_xFeO_{3-\delta}$ perovskite materials with other membrane materials, and it leads to an identification of the rate determining step of oxygen transport in relation with the nature of membrane materials. Table 1 shows the material acronyms of the membrane materials studied in this work.

Table 1: Composition and acronym of membrane materials, with corresponding color for each material in the figures 2, 5, 10, and 12.

Membrane materials	material acronyms	Color code
$Ba_{1-x}Sr_xFeO_{3-\delta}$	BSF	-
$SrFeO_{3-\delta}$	SF	Black
$Ba_{0.3}Sr_{0.7}FeO_{3-\delta}$	BSF37	Orange
$Ba_{0.5}Sr_{0.5}FeO_{3-\delta}$	BSF55	Green
$Ba_{0.7}Sr_{0.3}FeO_{3-\delta}$	BSF73	Red
$Ba_{0.9}Sr_{0.1}FeO_{3-\delta}$	BSF91	Blue
$BaFeO_{3-\delta}$	BF	Purple
$Ba_{0.5}Sr_{0.5}Co_{0.8}Fe_{0.2}O_{3-\delta}$	BSCF	-

2. Experimental part
2.1. BSF membrane samples

The $Ba_{1-x}Sr_xFeO_{3-\delta}$ (BSF) perovskite powders were synthesized by the citrate method and prepared from pure precursors of nitrate, i.e., $Ba(NO_3)_2$ (99+%, Alfa Aesar), $Sr(NO_3)_2$ (99.0% min, Alfa Aesar) and $Fe(NO_3)_3.9H_2O$ (98+%, Alfa Aesar). The stoichiometric amounts of the precursors were weighed and dissolved in deionized water under magnetic stirring. Citric acid was added to the solution with a molar ratio of citric acid and metal cation equal to 1.5:1. Ammoniac was added to the solution to control the pH, which was fixed at approximately 9.5. Then, the mixture was heated under stirring at 150°C to obtain a black gel. An ultra-porous powder was formed after calcination of the black gel at 300-350°C. Finally, this powder was calcined at 1050°C for 5 h to obtain the perovskite phase. The calcined perovskite powders were attrition-milled for 5 h in ethanol at 1100 rpm to obtain a suitable granulometry adapted to the tape-casting process. The perovskite powders after milling were treated at 850°C for 1 h to remove the eventual organic phases formed during the attrition-milling in a nylon bowl.

The BSF perovskite membranes were manufactured by the tape-casting process. The powder was milled in a planetary ball at high speed (260 rpm) for 1 h in an organic solvent (2-butanone/ethanol) with a dispersant (phosphate ester). Then, a methacrylate binder, Degalan

5107 (Röhm GmbH), and a plasticizer, phtalate dibutyl, were added to the perovskite suspension in a planetary ball at low rotation speed (130 rpm) for 12 h. The perovskite suspension was degased and casted onto a siliconed Mylar® film at 2.40 m.min^{-1} using a doctor blade. After solvent evaporation at room temperature, the 150-µm-thick green tapes were cut into 30-mm-diameter discs. These discs were stacked and laminated at 50°C under a pressure of 50 MPa to obtain membranes with a thickness of 1.30 mm and diameter of 24 mm after sintering. The green membranes were heated at 600°C to remove organic agents and then sintered to obtain a relative density higher than 95%. Table 2 shows the sintering conditions of the $Ba_{1-x}Sr_xFeO_{3-\delta}$ membrane samples. The study of sintering conditions is presented in section 3.2. Unfortunately, BSF73 perovskite material exhibited very low mechanical properties under air and nitrogen, and the oxygen semi-permeation under an air/argon gradient of BSF73 membranes could not be characterized in this work. Moreover, it was not possible to obtain cohesive $Ba_{1-x}Sr_xFeO_{3-\delta}$ F membranes for a range of compositions with x>0.7 (with x, the strontium rate). Therefore, oxygen semi-permeation performances were only measured for BSF37, BSF55 and BSF91 membranes. The relative density of the sintered membranes was measured by Archimedes' method.

Table 2: Sintering conditions of BSF membranes

Composition	Sintering conditions				Relative density
	Atmosphere	*Sintering temperature*	*Heating/cooling rate*	*Dwell time*	
BSF37	Air	1100°C	1°C/min	5 h	97%
BSF55	Air	1060°C	1°C/min	5 h	96%
BSF73	**Nitrogen**	**925°C**	**3°C/min**	**1 h**	**99%**
BSF91	Air	1140°C	1°C/min	5 h	97%

2.2. Characterization of membrane materials

X-ray diffraction analysis at room temperature were carried out on calcined powders with a D8 advance diffractometer with CuKα1, and the patterns were recorded in the 10-70° 2θ range with a step of 0.02° and exposure time of 1.1 s per step. The *in situ* evolution of $Ba_{0.7}Sr_{0.3}FeO_{3-\delta}$ (BSF73) perovskite structure was studied as a function of temperature in the

same conditions with an Anton Paar HTK1200N furnace. The heating and cooling rate was 5°C/min.

The powder was observed by scanning electron microscopy (SEM) field emission gun (LEO 1530 VP, Zeiss) to estimate the grain size. After sintering, the microstructure of the membranes was studied using scanning electron microscopy (JEOL IT 300 LV). The chemical compositions of $Ba_{0.3}Sr_{0.7}FeO_{3-\delta}$, $Ba_{0.5}Sr_{0.5}FeO_{3-\delta}$ and $Ba_{0.9}Sr_{0.1}FeO_{3-\delta}$ powders have been determined by ICP-AES, and the density of each powder has been measured by helium pycnometer (AccuPyc II 1340).

The sintering behaviour of BSF membranes was studied on pressed samples with a diameter of 10 mm using a dilatometer (TMA setsys 1600, Setaram instrumentation) from room temperature to 1200°C under air and nitrogen. The heating and cooling rate was 5°C/min.

2.3. Oxygen semi-permeation through BSF membranes

Fig. 1 shows the specific experimental setup used to measure oxygen semi-permeation fluxes and oxygen activities on both membrane surfaces [15, 16]. The membrane was sealed between two alumina tubes using gold rings at 960°C. The membrane was exposed to an oxygen partial pressures gradient: the feed side of the membrane (chamber 1) was flushed with an air flow of 100 ml/min, and the permeate side (chamber 2) was flushed with an argon flow of 200 ml/min. The oxygen partial pressures gradient through the membrane is the driving force for oxygen diffusion: oxygen migrates through the membrane from the feed side to the permeate side, while an electron flux moves in the opposite direction to preserve the electro-neutrality of the system. The third chamber was flushed with an argon flow to prevent eventual oxygen leakages. Between 600°C and 850°C, oxygen content in gas inlet and outlet (chamber 2) was measured using YSZ-oxygen sensors. These sensors provide an electromotive force that allows the determination of oxygen partial pressures from Nernst's law [15]. Thus, oxygen semi-permeation fluxes though the membrane sample is evaluated from oxygen partial pressures in the argon inlet and outlet. In both chambers 1 and 2, a system of microelectrodes, consisting of a gold electrode and zirconia point electrode, allows to measure the oxygen activities gradient between the gas and the membrane surface on both sides of the membrane.
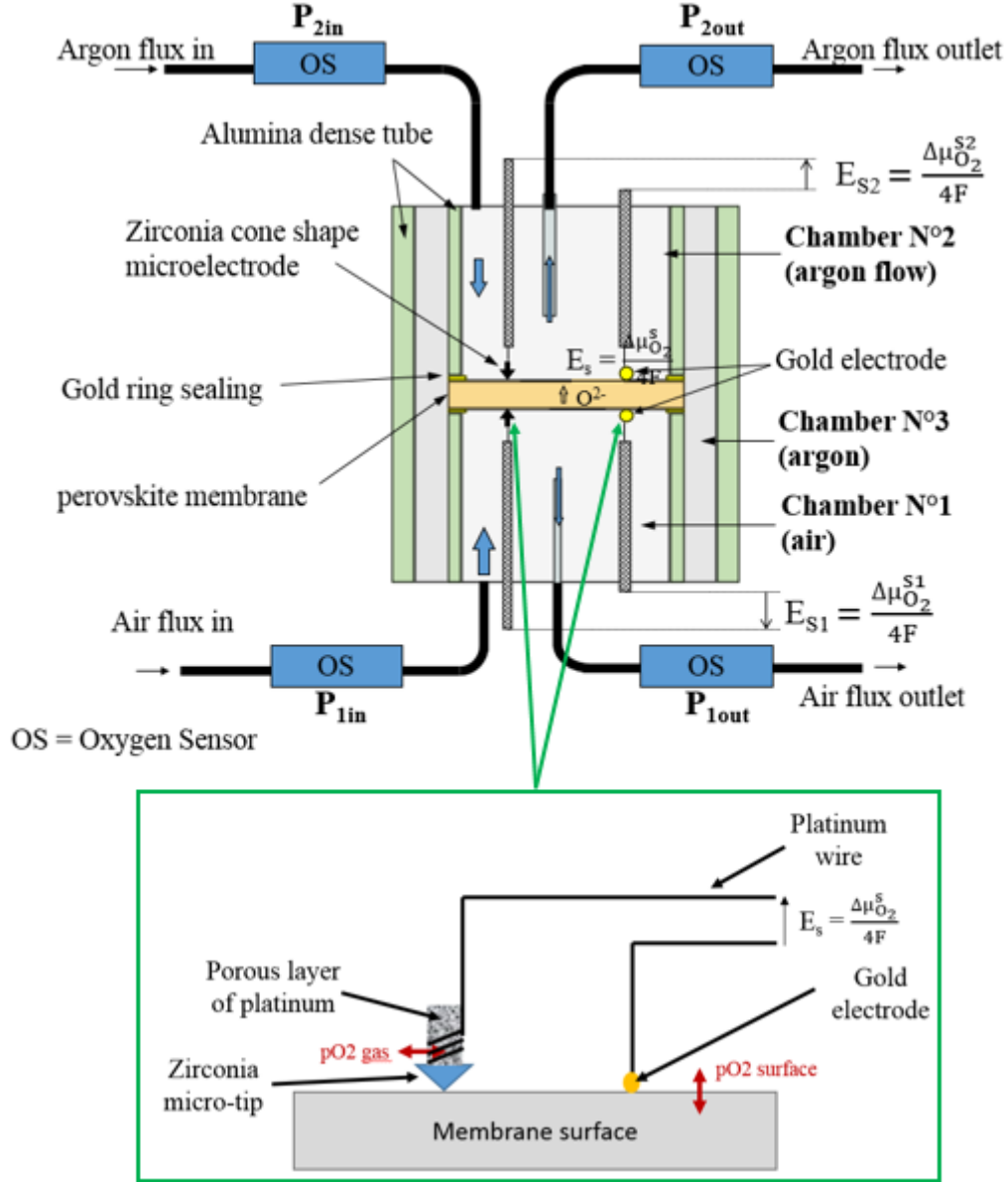
$$E_{S2} = \frac{\Delta\mu_{O_2}^{S2}}{4F}$$

$$E_s = \frac{\Delta\mu_{O_2}^{S}}{4F}$$

$$E_{S1} = \frac{\Delta\mu_{O_2}^{S1}}{4F}$$

$$E_s = \frac{\Delta\mu_{O_2}^{S}}{4F}$$

Fig. 1: Experimental setup for the measurement of oxygen fluxes and oxygen activities at the membrane surfaces

3. Results and discussion
3.1. Powder characterization

Fig. 2 shows the X-ray diffraction patterns of the synthesized BSF powders. BaFeO$_{3-\delta}$ powder (BF) has a perovskite phase of a rhombohedral structure and a secondary phase of an orthorhombic structure. However, Zhu et al. [17] have reported a hexagonal structure for BaFeO$_{3-\delta}$, but the material can exhibit different structures depending on the synthesis mode and the thermal treatment conditions of the powder [18]. The diffraction pattern of

$Ba_{0.9}Sr_{0.1}FeO_{3-\delta}$ (BSF91) shows a perovskite phase of cubic structure with a secondary phase of an orthorhombic structure, while the diffraction patterns of $Ba_{0.7}Sr_{0.3}FeO_{3-\delta}$ (BSF73), $Ba_{0.5}Sr_{0.5}FeO_{3-\delta}$ (BSF55) and $Ba_{0.3}Sr_{0.7}FeO_{3-\delta}$ (BSF37) powders show a pure perovskite phase with a cubic structure. These results are in good agreement with the data reported by Jaiswal et al. [18 for BSF materials. Nevertheless, the $SrFeO_3$ powder shows a tetragonal structure (pseudo-cubic structure), while Jaiswal et al. [18] have reported a cubic structure for $SrFeO_3$ perovskite.

The lattice parameter (a) was determined by FullProf software using the Lebail method and plotted as a function of the strontium amount x in Fig. 3 for cubic and tetragonal (pseudo-cubic) structures. The lattice parameter decreases linearly with the strontium amount, which is in good agreement with the work reported by Jaiswal et al. [18]. However, the lattice parameter values obtained in this work for x = 0.8 and 0.9 are smaller than those obtained by Jaiswal et al. [18] for similar material compositions, potentially due to the variation of the oxygen understoichiometry in the perovskite structure. This phenomenon is linked to the heat treatment conditions, which can induce a chemical expansion of the material [18, 19].
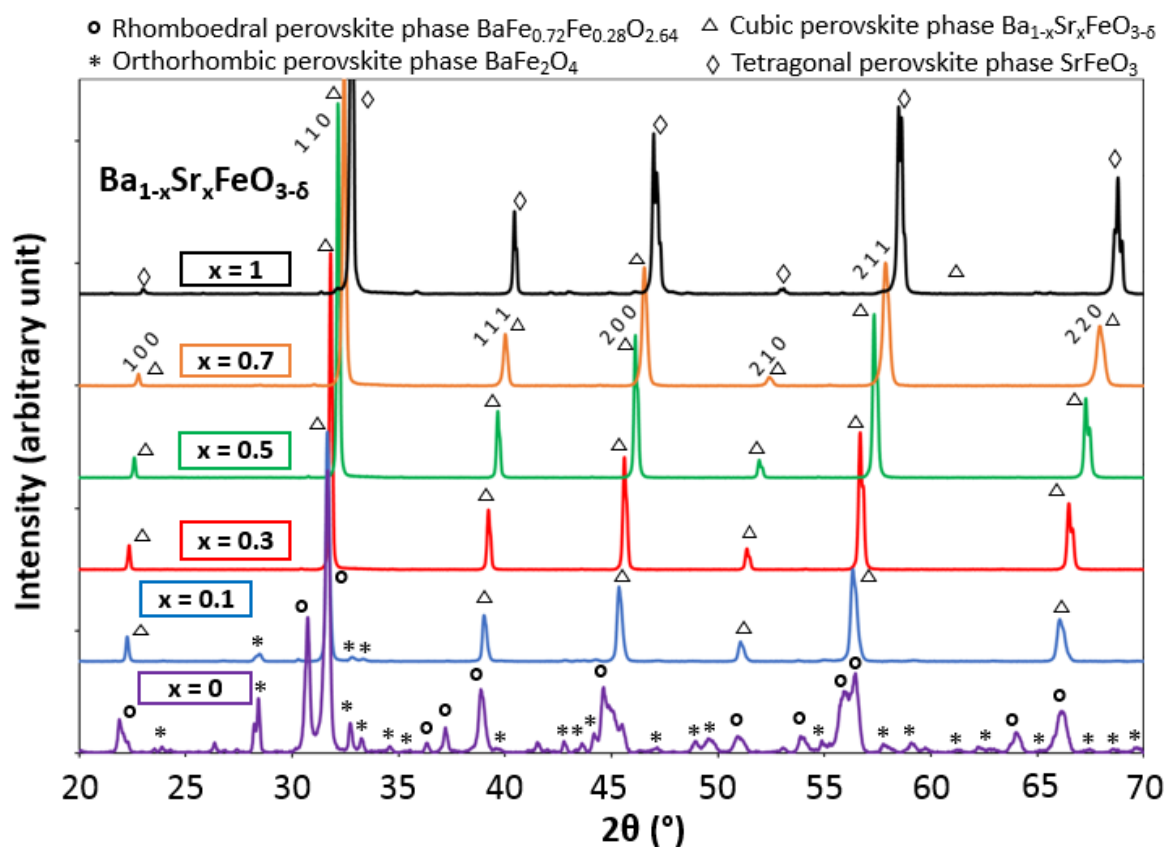
Fig. 2: X-ray diffraction patterns of Ba$_{1-x}$Sr$_x$FeO$_{3-\delta}$ powders, with 0<x<1
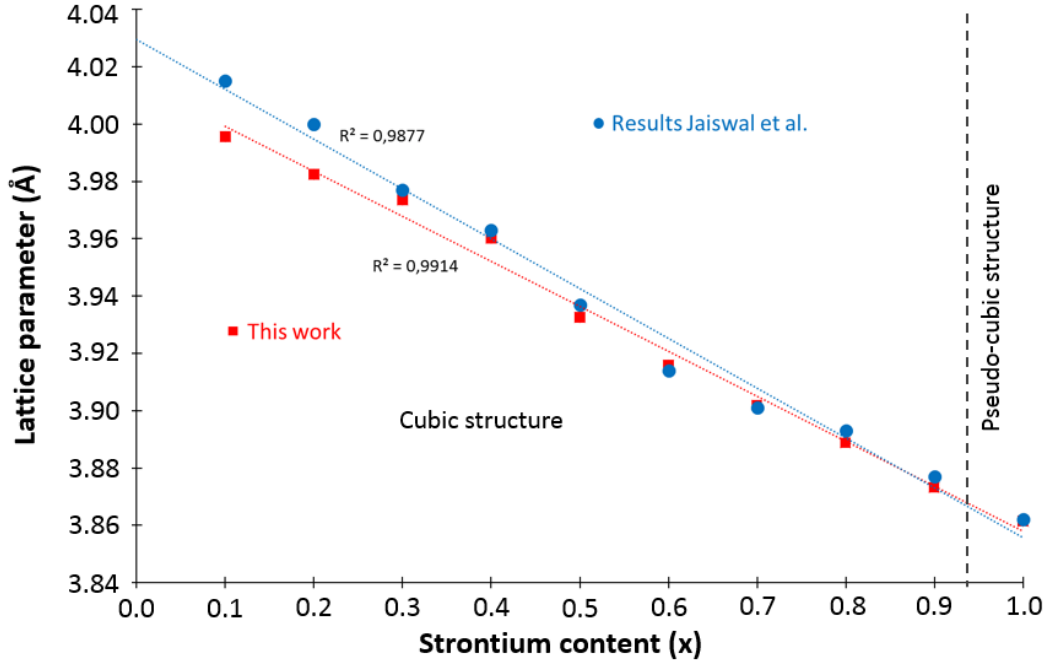

Fig. 3: Lattice parameter values of BSF perovskite materials

Table 3 shows the stoichiometric proportions that have been measured for barium, strontium and iron. The zirconium traces have been detected in the synthesized powders, which is likely linked to the pollution of attrition balls during the grinding step. It notes that the measured stoichiometric proportions (x, y) are very close to the expected values, and zirconium contamination by attrition balls is very low (Zr contamination < 50 ppm in weight).

Table 3: ICP-AES results for the synthesized powders

Elements	x, y evaluated by ICP analysis in Ba$_{1-x}$Sr$_x$Fe$_y$O$_{3-\delta}$	x, y expected in Ba$_{1-x}$Sr$_x$Fe$_y$O$_{3-\delta}$	Relative error %
BSF37			
Ba	1-x = 0.31	1-x = 0.3	1.9%
Sr	x = 0.69	x= 0.7	1.3%
Fe	y = 1	y = 1	1.6%
BSF55			
Ba	1-x = 0.50	1-x = 0.5	1.1%
Sr	x = 0.49	x= 0.5	1.5%

Fe	y = 1	y = 1	1.3%
BSF91			
Ba	1-x = 0.9	1-x = 0.9	0.7%
Sr	x = 0.1	x = 0.1	1.5%
Fe	y = 0.99	y = 1	1.1%

Fig. 4 shows the SEM micrographs of a typical powder before and after attrition-milling and thermal treatment at 850°C. The synthesized powder is composed of ultra-porous large agglomerates (approximately 30 μm on average). After attrition-milling, agglomerates were broken, and the grain size was reduced down to an average size less than 1 μm, which is adapted to the tape-casting process.
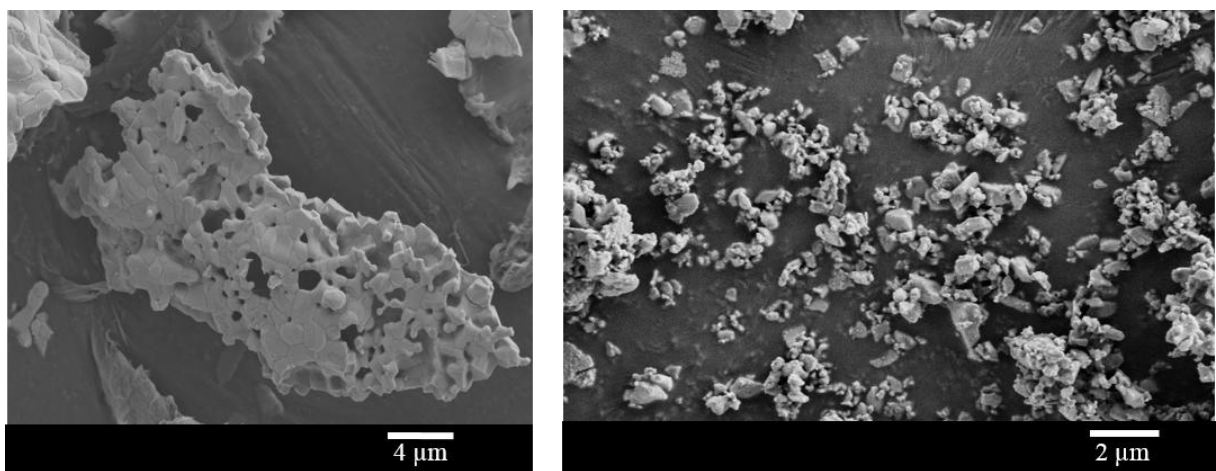
Fig. 4: SEM micrographs of the initial synthesized powder (left) and of the powder after attrition-milling and thermal treatment (right)

As expected, the density of perovskite powders increases with Ba content, except for BSF91 and BF. Indeed, the densities of the BSF91 and BF powders here are significantly lower than the theoretical densities, likely due to the presence of secondary phases in these two powders (Table 4).

Table 4: Density of BSF powders

Composition	SF (pure)	BSF37 (pure)	BSF55 (pure)	BSF73 (pure)	BSF91 (not pure)	BF (not pure)
Density (g.cm^{-3})	5.36 ±0.02	5.47 ±0.02	5.62 ±0.02	5.80 ±0.02	5.77 ±0.02	5.64 ±0.02
Theoretical density* (g.cm^{-3})	5.36	5.61	5.75	5.84	6.00	6.10**

*The theoretical density of the $Ba_{1-x}Sr_xFeO_{3-\delta}$ perovskite series is evaluated with $\delta = 0.36$, as reported in [17]

3.2. Membrane sintering

Four BSF compositions (BSF37, BSF55, BSF73 and BSF91) have been studied to define optimal sintering conditions. Green pressed samples of these four compositions were analysed using a dilatometer under air. Fig. 5 shows the dilatometric curves of the BSF55 and BSF73 pressed samples. Two expansions are observed for these two materials under air, a first expansion at approximately 200-250°C and a second one at 400-450°C. The second expansion is particularly important for BSF73 in comparison to the three other BSF materials measured. The X-ray diffraction patterns (Fig. 6) show a phase transition for BSF73 material at approximately 200°C and a second one at 350-450°C. The BSF73 material shows a brownmillerite structure between 200°C and 450°C and a cubic structure up to 450°C. Additionally, McIntosh et al. [19] showed a similar behaviour for $SrCo_{0.8}Fe_{0.2}0_{3-\delta}$ (SCF82) material. SCF82 material under nitrogen shows a brownmillerite structure with a formula of $Sr_2Co_{1.2}Fe_{0.4}O_5$ at 300°C, which corresponds to a decrease in oxygen stoichiometry and ordering of oxygen vacancies in a crystallographic axis. Between 700 and 800°C, SCF82 material has a cubic structure. These structures are associated with an order or disorder of oxygen vacancies in the perovskite structure. BSCF material has a cubic structure on a large range of temperature under nitrogen and air.

The thermal expansion coefficient (TEC) of BSF materials were determined from dilatometer curves during cooling. It is approximately of 18 10^{-6} K^{-1} at low temperature (50°C-400°C) and approximately of 28 10^{-6} K^{-1} at high temperature (800°C-1200°C), which is higher than the TEC of BSCF material (11.5 10^{-6} on average [20] and 24 10^{-6} K^{-1} at high temperature[21, 19]]). However, but the TEC of BSF materials is still close to the TEC of SCF material (17.9 10^{-6} K^{-1} on average [20] and 30 10^{-6} K^{-1} at high temperature [21, 19]).

The TEC of BSF73 material was also studied under nitrogen to understand the impact of pO_2 surrounding gas on the expansion observed under air, particularly from 400-450°C. This large thermal expansion can be associated with the phase transition brownmillerite-cubic under air, as reported on X-ray diffraction patterns versus temperature on Fig. 6. No phase transition and thermal expansion are observed at approximately 400°C under nitrogen for BSF73 material as reported in Fig. 5 and 7. Thus, under nitrogen, the BSF materials show a brownmillerite structure from 200°C to 1000°C (Fig. 7), and the sintering mechanisms are activated at lower temperature under nitrogen than under air (Fig. 5). Fig. 8 shows the different structures of BSF73 material in relation to the temperature and the pO_2 of the surrounding atmosphere from

the X-ray diffraction patterns obtained at different temperatures under air and nitrogen (Fig. 6 and 7). The sintering of BSF materials under nitrogen prevents the large thermal expansion at approximately 400°C, limiting the risk of cracking during the sintering of membranes. Nevertheless, the sintered membranes are exposed to a gradient of oxygen partial pressures during the semi-permeation measurements (commonly 0.21 / 10^{-3} atm. or close to the oxygen partial pressure in air). When the membrane is sintered under nitrogen, there is a large chemical expansion at the membrane surface in contact with air, which leads to a cracking of membranes during the semi-permeation measurements. Then, the solution consists of sintering BSF membranes under air with low heating and cooling rates to prevent the cracking of the membrane during the semi-permeation tests [10].
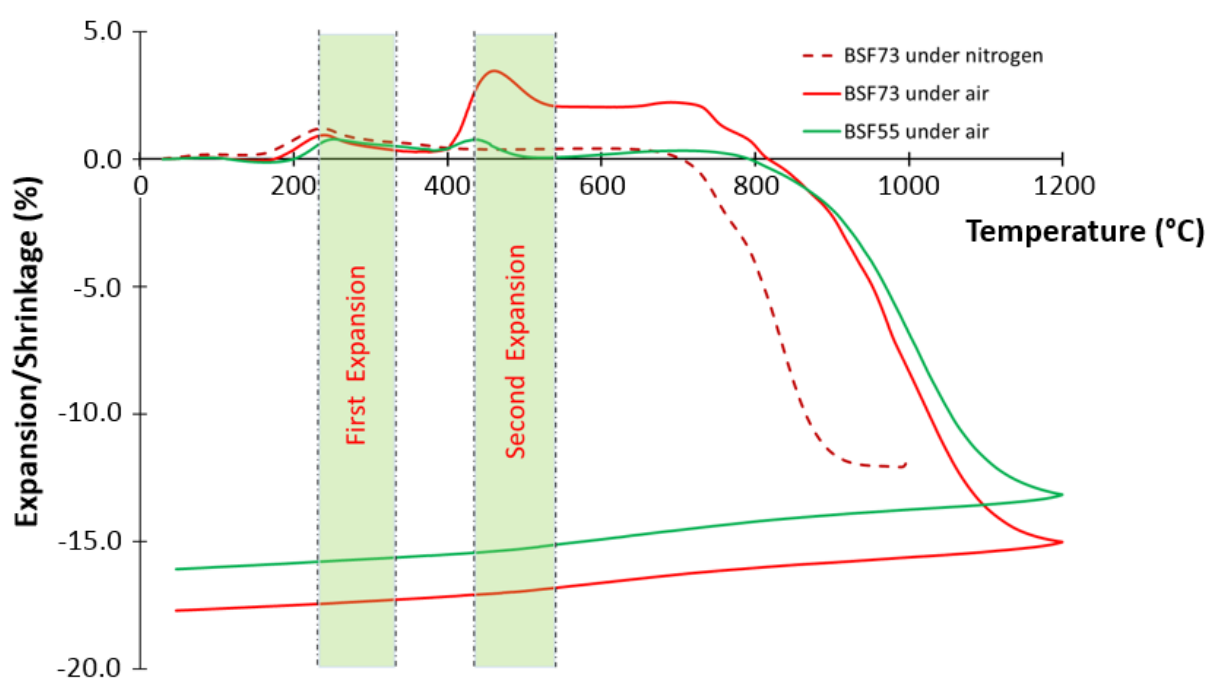
Fig. 5: Dilatometric curves under air and nitrogen of BSF73 and BSF55 samples
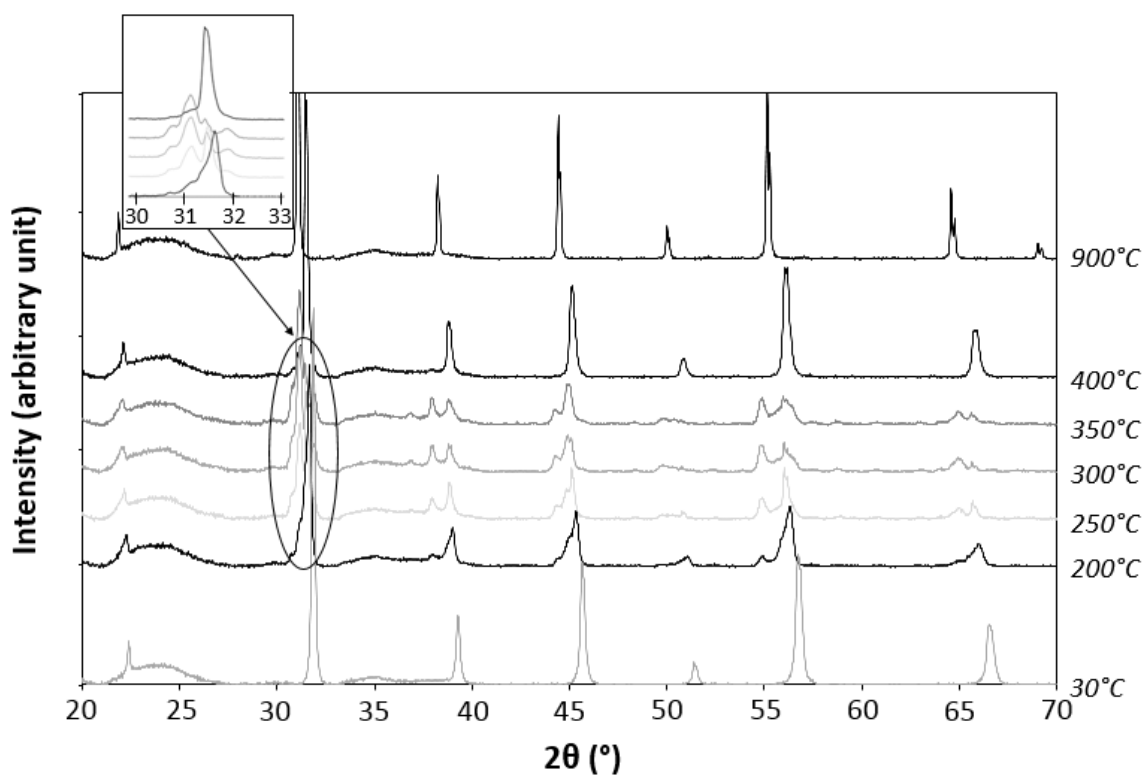
Fig. 6: X-ray diffraction patterns under air of BSF73 powder between 30°C and 900°C
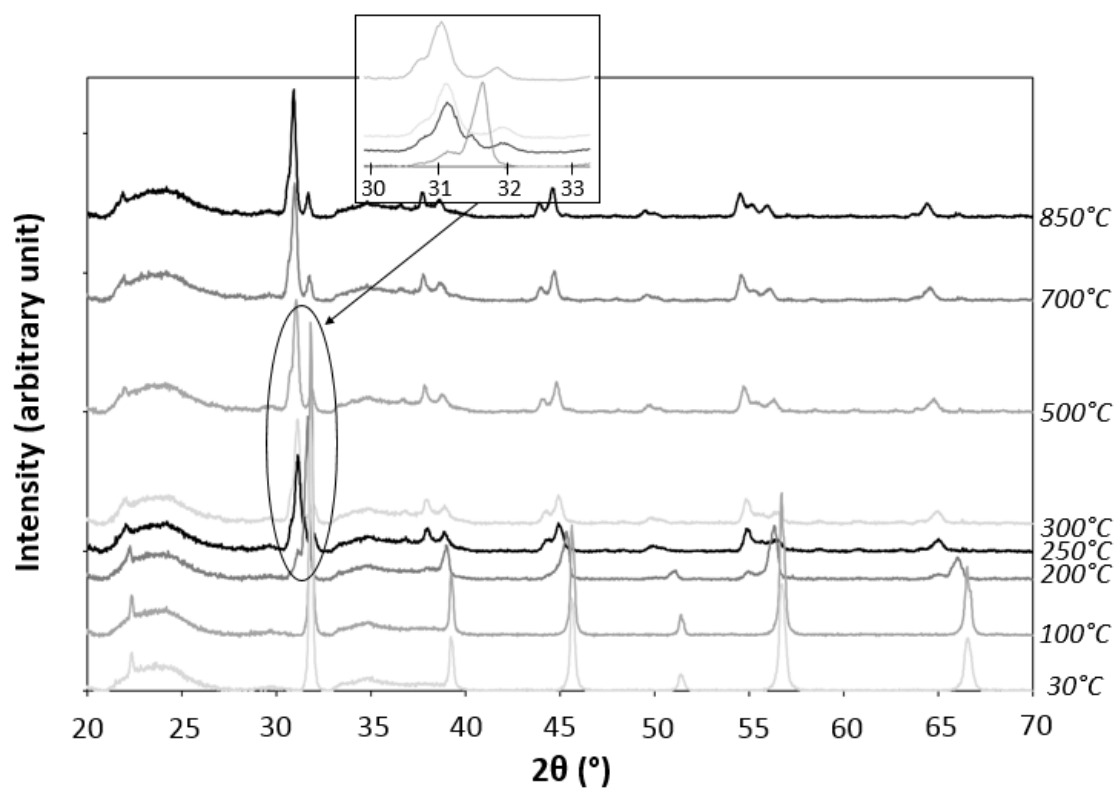

Fig. 7: X-ray diffraction patterns under nitrogen of BSF73 powder between 30°C and 850°C
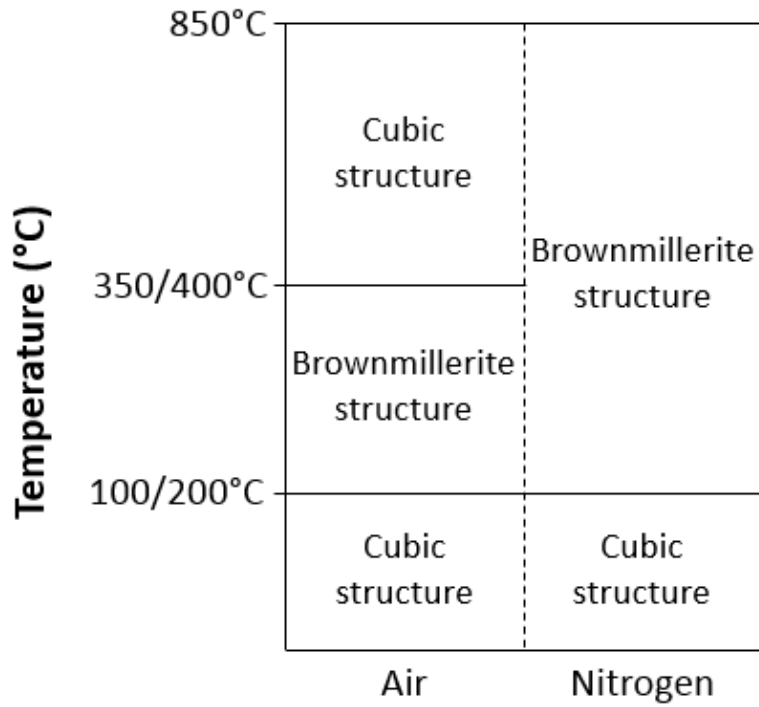
Fig. 8: Nature of the BSF73 powder structure up to 850°C under different gases

Fig. 9 shows the microstructures at the surface of SF, BSF19, BSF37, BSF55 and BSF91 membranes. There is few micro-porosities at the membrane surfaces, which is in agreement with the relative density of the membrane samples. This residual porosity is likely linked to residual agglomerates after the milling step [3]. The average grain size is higher for SF, BSF19 and BSF37 materials (Table 5). It can also be assumed that the potential Sr segregation at the grain boundaries in BSF materials can increase the grain boundaries mobility and grain growth during the last step of sintering at high temperature [22]. The cross section of the BSF37 membrane, in Fig. 9 d), shows that the rate of micro-porosities in the membrane bulk is also very low, and there is no delamination between layers after sintering. The microstructural observations of other BSF membranes in bulk, shows also few micro-porosities and no delamination between layers after sintering.
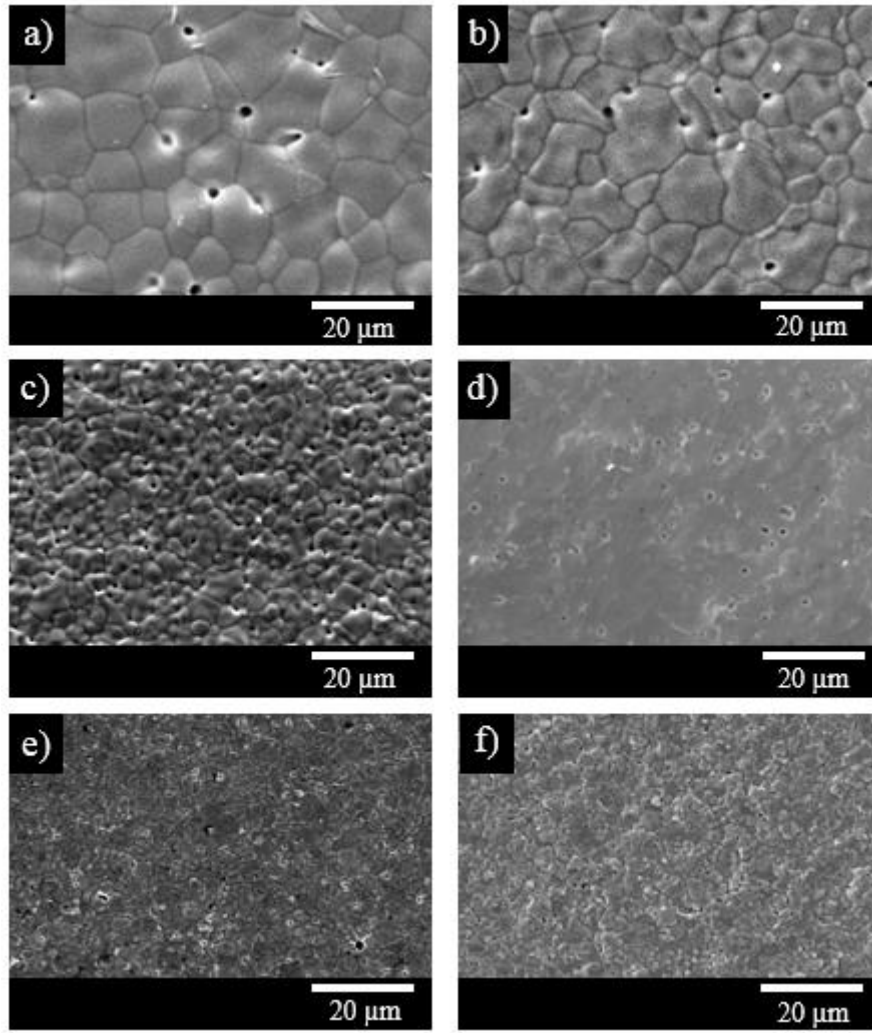
Fig. 9: SEM micrographs of the membranes surface for a) SF b) BSF19, c) BSF37, e) BSF55 and f) BSF91 and micrograph of cross section for d) BSF37

Table 5: Grain size of BSF membranes

Composition	Grain size range (µm)
SF	2.5-20
BSF19	2.5-15
BSF37	2-10
BSF55	1.5-5
BSF91	2-5

3.3. Electrochemical performances through BSF membranes

3.3.1. Oxygen semi-permeation fluxes

Fig. 10 shows the evolution of oxygen semi-permeation fluxes versus the temperature for the BSF membrane materials. The highest oxygen flux was obtained for BSF91 membrane with 4.1 10^{-3} mol.m^{-2}.s^{-1} at 850°C, and the oxygen flux of BSF samples increases with barium content (Table 6). The same observation has been reported by Jaiswal et al. [10] for these compositions. Teraoka et al. [11] reported that the oxygen flux through $Ba_xSr_{1-x}Fe_{0.9}Mn_{0.1}O_{3-\delta}$ (x = 0; 0.1;...; 0.5) membranes increased with barium content until x = 0.3 (BSFMn3791) and then decreased. These observations also assume that the increase in oxygen flux with barium content is likely linked to the nature of doping elements in the B site of perovskite structure.

The oxygen semi-permeation fluxes through BSF membranes are 2-3 times lower than the fluxes obtained with BSCF membranes with similar thickness and measurement conditions [23], or 2-4 times lower than the fluxes reported by Klande et al. [12] for BSCF membranes, which correspond to membrane materials with one of the best oxygen semi-permeation performances in the literature (Table 6). The oxygen fluxes through BSF37, BSF55 and BSF91 membranes in this work are 4-7 times lower than the oxygen fluxes reported by Teraoka et al. [11] and Jaiswal et al. [10] for a similar composition of membrane material.

These variations of oxygen semi-permeation performances for a similar material could be linked to the oxygen semi-permeation measurement conditions [14] and to the microstructure (grain size, as reported in Table 5) of the membrane material [23]. Indeed, some studies have demonstrated the influence of the microstructure (starting powder, green density, sintering conditions) on the oxygen semi-permeation performances through BSCF membranes. For instance, Reichmann et al. [23] have reported that the oxygen permeation flux through the BSCF membrane was limited by bulk diffusion, and therefore, a large grain size allows enhanced oxygen fluxes through the membrane. Klande et al. [12] have also reported the same observation. Arnold et al. [24] have studied the influence of sintering doping on grain growth and have reported the same phenomenon.
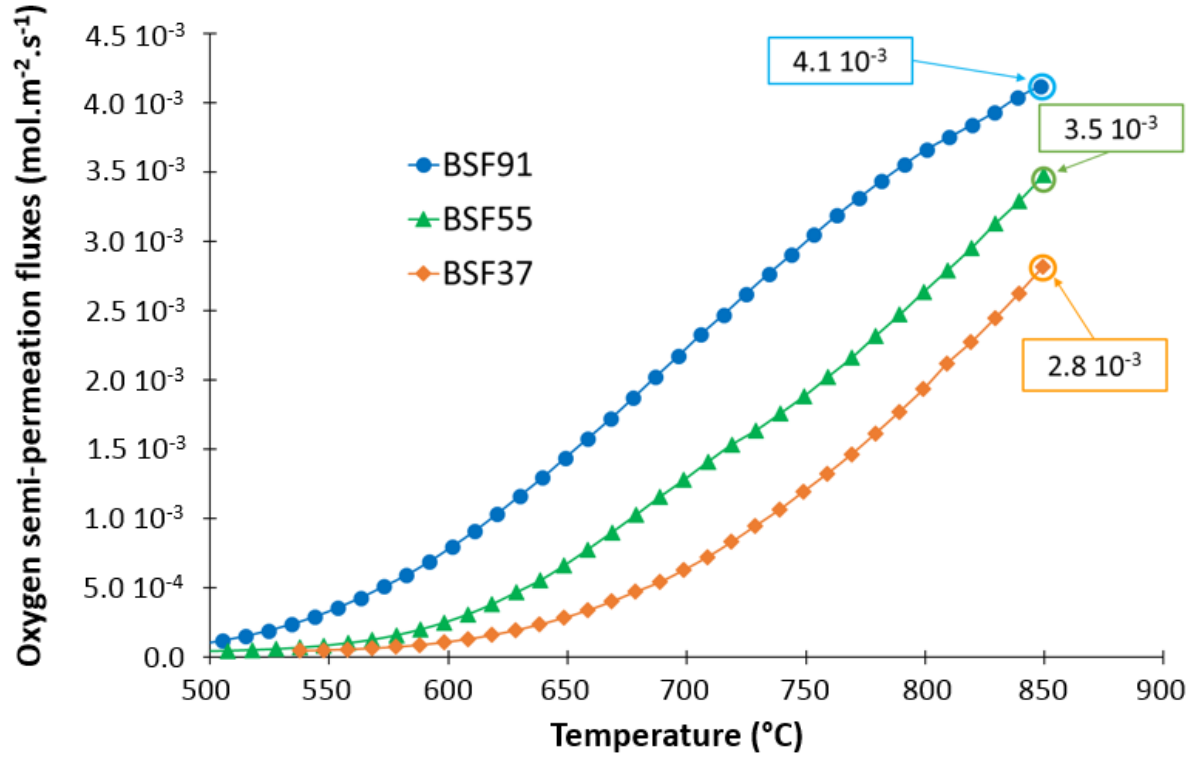
Fig. 10: Temperature dependence of the oxygen semi-permeation fluxes through dense BSF membranes under an air (100 ml.min^{-1})/argon (200 ml.min^{-1}) gradient

Table 6: Oxygen semi-permeation fluxes for BSF and BSCF membranes at 850°C

Material	Reference	Membrane thickness/ grain size range	pO$_2$ at the oxygen rich chamber/ oxygen lean chamber (atm.)	Oxygen semi-permeation flux (mol.m^{-2}.s^{-1})
BSF37	Teraoka et al. [11]	1 mm/-	Air/Helium	1.8 10^{-2}
BSF37	Jaiswal et al. [10]	1 mm/-	Air/Argon	1.5 10^{-2}
BSF37	This work	1.3 mm/2-10 μm	0.21/5.7 10^{-3}	2.8 10^{-3}
BSF55		1.3 mm/1.5-5 μm	0.21/7.0 10^{-3}	3.5 10^{-3}
BSF55	Jaiswal et al. [10]	1 mm/-	Air/Argon	1.7 10^{-2}
BSF91	This work	1.3 mm/2-5 μm	0.21/8.3 10^{-3}	4.1 10^{-3}
BSF91	Jaiswal et al. [10]	1 mm/-	Air/Argon	1.8 10^{-2}
BSCF	Klande et al. [12]	-/13.9 μm	Air/Helium-Neon	1 10^{-2}

16

| BSCF | Reichmann et al. [23] | 1 mm/8-12 μm | 0.21/1.5 10^{-2} | 7-8 10^{-3} |

3.3.2. *Oxygen diffusion and surface exchange coefficients*

As reported in our previous works [15, 16], the oxygen diffusion coefficient D_O and the oxygen incorporation and oxygen desorption coefficients, k_i and k_d respectively, are evaluated from the oxygen flux and the gradient of oxygen chemical potentials through the surface of the membrane as follows:

$$D_O = \frac{4RTL J_{O_2}}{C_O \Delta\mu_{O_2}^{bulk}} \qquad \text{Eq. (1)}$$

$$k_i = 2J_{O_2} \Big/ \left(C_O \left(\exp\left(\frac{(1-n)\Delta\mu_{O_2}^i}{RT}\right) - \exp\left(\frac{-n\Delta\mu_{O_2}^i}{RT}\right) \right) \right) \qquad \text{Eq. (2)}$$

$$k_d = 2J_{O_2} \Big/ \left(C_O \left(\exp\left(\frac{(1-n)\Delta\mu_{O_2}^d}{RT}\right) - \exp\left(\frac{-n\Delta\Delta\mu_{O_2}^d}{RT}\right) \right) \right) \qquad \text{Eq. (3)}$$

with L: membrane thickness, J_{O_2}: oxygen semi-permeation flux through the membrane, C_O: molar oxygen concentration in the membrane, $\Delta\mu_{O_2}^{bulk}$: gradient of oxygen chemical potentials through the membrane bulk (Fig. 12 a), $\Delta\mu_{O_2}^i$: gradient of oxygen chemical potentials between the gas at the vicinity of the oxygen rich surface and the membrane bulk close to the oxygen rich surface (Fig. 12 a), $\Delta\mu_{O_2}^d$: gradient of oxygen chemical potentials between the gas at the vicinity of the oxygen lean surface and the membrane bulk close to the oxygen lean surface (Fig. 12 a), n: exponent coefficient, constant between 0 and 1 (n = 0.5 for mixed conductors).

Table 7 shows the coefficients D_O (or D*) and k_d (or k*) obtained using the oxygen semi-permeation method (or isotopic exchange method) for $Ba_{1-x}Sr_xFeO_{3-\delta}$ perovskite and $Ba_{0.5}Sr_{0.5}Co_{0.8}Fe_{0.2}O_{3-\delta}$ perovskite materials. There is a slight apparent discrepancy between coefficients D_O and D* obtained using the oxygen semi-permeation [23, 25] and isotopic exchange [13] methods for a similar material, i.e., $Ba_{0.5}Sr_{0.5}Co_{0.8}Fe_{0.2}O_{3-\delta}$ perovskite. The same apparent discrepancy is observed between the coefficients k_d and k* obtained using the oxygen semi-permeation and isotopic exchange methods, mainly due to experimental conditions used by these two methods. In particular, the oxygen permeation method involves

17

a system that is far from equilibrium, while in case of the isotopic exchange method, the system is at chemical equilibrium. However, the k_d coefficient obtained using the semi-permeation method [23, 25] has the same order of magnitude as the k* coefficient obtained by the isotopic exchange method [13], respectively 5.5 10^{-6} and 2.6 10^{-6} cm.s^{-1} for Ba$_{0.5}$Sr$_{0.5}$Co$_{0.8}$Fe$_{0.2}$O$_{3-\delta}$ perovskite at pO$_2$ = 1.2-1.5 10^{-2} atm. and 800°C. The oxygen incorporation coefficient (k_i) is higher by one order of magnitude or almost than oxygen desorption coefficient (k_d) and the coefficient obtained by isotopic exchange (k*). This means that the kinetics of oxygen desorption reactions are slower than the kinetics of oxygen incorporation reactions.

From the data obtained by the semi-permeation method, the k_d coefficients of Ba$_{1-x}$Sr$_x$FeO$_{3-\delta}$ perovskite materials increase with the strontium content. Those obtained for Ba$_{0.3}$Sr$_{0.7}$FeO$_{3-\delta}$ and Ba$_{0.5}$Sr$_{0.5}$FeO$_{3-\delta}$ membranes are high and similar to those reported for Ba$_{0.5}$Sr$_{0.5}$Co$_{0.8}$Fe$_{0.2}$O$_{3-\delta}$ perovskite [23, 25], which suggests that these materials are potential coating materials to improve the surface exchange kinetics of the membrane. Conversely, the D$_O$ coefficients of Ba$_{0.3}$Sr$_{0.7}$FeO$_{3-\delta}$ and Ba$_{0.5}$Sr$_{0.5}$FeO$_{3-\delta}$ membranes are lower by almost one order of magnitude compared with the one of Ba$_{0.5}$Sr$_{0.5}$Co$_{0.8}$Fe$_{0.2}$O$_{3-\delta}$ perovskite. However, as expected, the D$_O$ coefficient increases with the Ba content. Indeed, the increase in the lattice parameter (a) linked to Ba content (Fig. 3) likely leads to an increase in oxygen mobility and/or an increase in the dimensions of the oxygen conduction pathway in the perovskite structure [26].

Table 7: Oxygen bulk diffusion and exchange surface coefficients for BSF and BSCF membranes

Material	Reference	pO$_2$ at the oxygen lean chamber (atm.) or at condition measurements *Temperature*	D$_O$ (or D*) (cm^2.s^{-1})	k$_i$ (or k*) (cm.s^{-1})	k$_d$ (or k*) (cm.s^{-1})
BSF37	This work (semi permeation)	5.7 10^{-3} *850°C*	3.6 (±1) 10^{-7}	1.3 (±0.5) 10^{-4}	1.2 (±0.5) 10^{-5}
BSF55		7.0 10^{-3} *850°C*	5.6 (±1) 10^{-7}	1.0 (±0.5) 10^{-4}	8.7 (±2) 10^{-6}
BSF91		8.3 10^{-3} *850°C*	1.4 (±0.5) 10^{-6}	1.8 (±0.5) 10^{-4}	4.8 (±1) 10^{-6}

BSCF	Reichmann et al. [23, 25]] (semi-permeation)	$1.5 \ 10^{-2}$ *850°C*	$2.9 \ (\pm0.5) \ 10^{-6}$	$8.3 \ (\pm2) \ 10^{-5}$	$9.3 \ (\pm2) \ 10^{-6}$
		$1.2 \ 10^{-2}$ *800°C*	$2.1 \ (\pm0.5) \ 10^{-6}$	$5.3 \ (\pm1) \ 10^{-5}$	$5.5 \ (\pm1) \ 10^{-6}$
BSCF	Berenov et al. [13] (isotopic exchange)	$7.5 \ 10^{-3}$ *800°C*	(D*) $6.8 \ (\pm0.2) \ 10^{-7}$	(k*) $1.4 \ (\pm0.1) \ 10^{-6}$	
		$1.5 \ 10^{-2}$ *800°C*	(D*) $5.6 \ (\pm0.2) \ 10^{-7}$	(k*) $2.6 \ (\pm0.1) \ 10^{-6}$	

3.3.3. Activation energies of oxygen semi-permeation fluxes

Fig. 11 shows the Arrhenius plots of oxygen semi-permeation fluxes versus 1/T (T: absolute temperature in K). The slope of the Arrhenius plot allows to evaluate the activation energy (Ea) of the mechanism limiting oxygen transport through the membrane.

There is an abrupt variation of the slope of the Arrhenius plots for the three BSF membranes between 650-750°C. This variation of Ea could likely correspond to an evolution of the nature of the limiting step (rds) of oxygen transport through the membrane with temperature. At high temperature (>800°C), the profile of the oxygen chemical potential for the BSF membranes in Fig. 12 clearly shows a large oxygen chemical potentials gradient through the membrane bulk, which suggests that the oxygen semi-permeation flux is governed by the oxygen bulk diffusion at high temperature. At low temperature (<600°C), the highest activation energy corresponds to the activation energy of oxygen exchanges surface mechanisms [15] (Table 8). A similar behaviour was observed for $La_2NiO_{4+\delta}$ membranes in a previous work [27].

At high temperature, the activation energy of the oxygen flux corresponding to oxygen bulk diffusion mechanisms, decreases when the Ba content increases. This activation energy is close to 40 kJ.mol^{-1} for BSF91 membranes (Table 8). This value is very close to the activation energy of oxygen flux reported at high temperature (775-950°C) for BSCF membranes by Shao et al. [28] and Reichmann et al. [23, 25]. However, at low temperature (600-775°C), Shao et al. [28] reported a lower activation energy of 72.6 kJ.mol^{-1} for BSCF membranes than the one obtained in this work for BSF91 membrane (i.e., 120 kJ.mol^{-1}). Moreover, for BSF membranes, there is not clear evolution of activation energy at low temperature with the Ba content. Indeed, there is a low variation of activation energy at low temperature with Ba content, varying from 120 to 170 kJ.mol^{-1}.
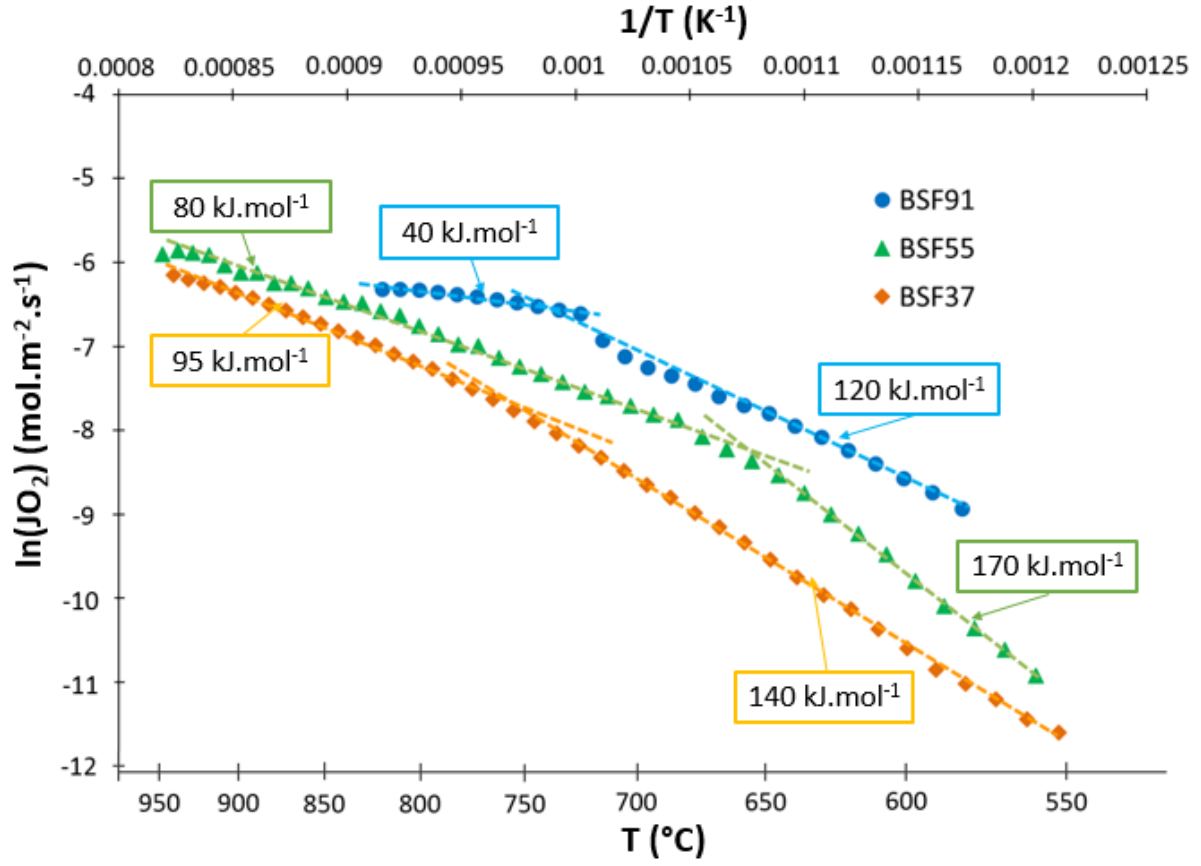
Fig. 11: *Arrhenius plots of oxygen fluxes* versus *1/T for BSF37, BSF55 and BSF91 membranes*
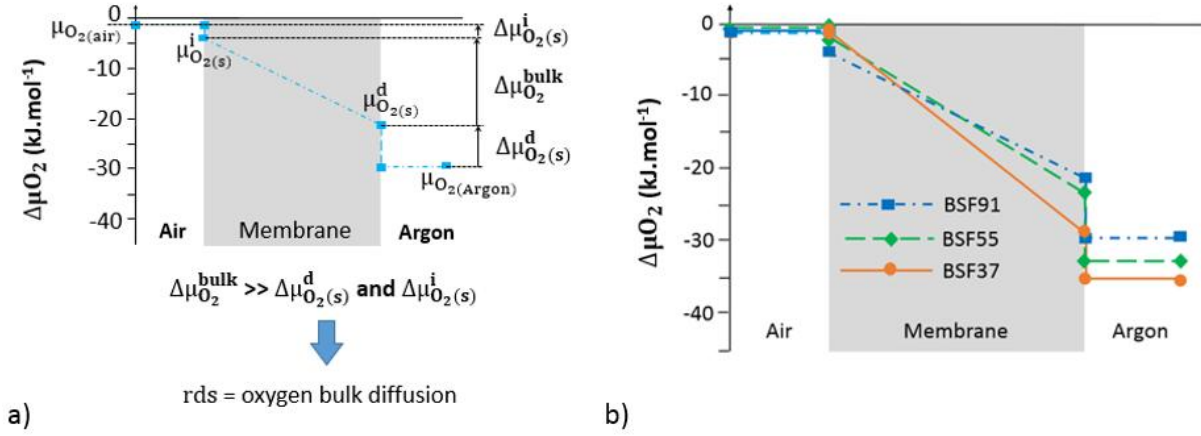

Fig. 12: *Profile of the oxygen chemical potential through BSF91 perovskite membrane at 800°C with three main steps: oxygen incorporation, bulk diffusion, and desorption, b) Profiles of the oxygen chemical potential through BSF37, BSF55 and BSF91 membranes at 800°C*

Table 8: Activation energies of the oxygen transport mechanisms for BSF and BSCF membranes

Material	Reference	Ea (500°C-700°C)	Ea (700°C-1000°C)
BSF37	This work	140 kJ.mol^{-1}	95 kJ.mol^{-1}
BSF55		170 kJ.mol^{-1}	80 kJ.mol^{-1}
BSF91		120 kJ.mol^{-1}	40 kJ.mol^{-1}
BSCF	Reichmann et al. [23, 25]	65 kJ.mol^{-1}	40 kJ.mol^{-1}

4. Conclusion

This study shows that the oxygen flux performances collected in the literature for the $Ba_{1-x}.Sr_xFeO_{3-\delta}$ perovskite membranes can be affected by a large spreading of values linked mainly to the potential gas leakages through the membrane or low relative density of membrane materials (< 95%). Then, this work gives to measure directly oxygen diffusion and surface exchange coefficients of BSF materials by a specific method based on the oxygen permeation and the oxygen activity measurements at the membrane surfaces.

$Ba_{1-x}.Sr_xFeO_{3-\delta}$ (BSF) perovskites, corresponding to free cobalt materials to improve chemical stability at high temperature and under low oxygen partial pressures for oxygen semi-permeation membranes, show a high oxygen desorption coefficient, slightly lower or similar to those reported for $Ba_{0.5}Sr_{0.5}Co_{0.8}Fe_{0.2}O_{3-\delta}$ (BSCF) material. This k_d (oxygen desorption coefficient) increases with the strontium content in BSF materials, while the oxygen diffusion coefficient decreases significantly with the strontium content at 850°C.

Additionally, the oxygen semi-permeation fluxes of BSF membranes (1.3 mm in thickness) are governed by the oxygen bulk diffusion at high temperature (above 800°C) and by oxygen desorption mechanisms at low temperature (below 600°C).

Unfortunately, BSF materials show two large thermal expansions in air due to phase transitions with temperature. These expansions are detrimental for the cohesion of the material during sintering, with a high risk of membrane cracking during sintering and in operating conditions. Additionally, the BSF materials show low mechanical properties, such as BSCF materials. It was not possible to obtain cohesive BSF membranes for a range of compositions with x>0.7, which is a critical point for potential industrial applications of BSCF or BSF materials as dense membrane materials for oxygen transport membranes.

Nevertheless, $Ba_{1-x}Sr_xFeO_{3-\delta}$ perovskites are promising materials as coating layers at the surface of oxygen transport membranes due to the high oxygen desorption coefficient.

5. References

[1] M. Arnold, H. Wang, A. Feldhoff, Influence of CO2 on the oxygen permeation performance and the microstructure of perovskite-type (Ba0.5Sr0.5)(Co0.8Fe0.2)O3−δ membranes, J. Membr. Sci. 293 (2007) 44–52. https://doi.org/10.1016/j.memsci.2007.01.032.

[2] C. Buysse, A. Kovalevsky, F. Snijkers, A. Buekenhoudt, S. Mullens, J. Luyten, J. Kretzschmar, S. Lenaerts, Development, performance and stability of sulfur-free, macrovoid-free BSCF capillaries for high temperature oxygen separation from air, J. Membr. Sci. 372 (2011) 239–248. https://doi.org/10.1016/j.memsci.2011.02.011.

[3] S. Baumann, F. Schulze-Küppers, S. Roitsch, M. Betz, M. Zwick, E.M. Pfaff, W.A. Meulenberg, J. Mayer, D. Stöver, Influence of sintering conditions on microstructure and oxygen permeation of Ba0.5Sr0.5Co0.8Fe0.2O3−δ (BSCF) oxygen transport membranes, J. Membr. Sci. 359 (2010) 102–109. https://doi.org/10.1016/j.memsci.2010.02.002.

[4] O. Ravkina, T. Klande, A. Feldhoff, Investigation of Zr-doped BSCF perovskite membrane for oxygen separation in the intermediate temperature range, J. Solid State Chem. 201 (2013) 101–106. https://doi.org/10.1016/j.jssc.2013.02.023.

[5] S.M. Fang, C.-Y. Yoo, H.J.M. Bouwmeester, Performance and stability of niobium-substituted Ba0.5Sr0.5Co0.8Fe0.2O3−δ membranes, Solid State Ion. 195 (2011) 1–6. https://doi.org/10.1016/j.ssi.2011.05.022.

[6] P. Haworth, S. Smart, J. Glasscock, J.C. Diniz da Costa, Yttrium doped BSCF membranes for oxygen separation, Sep. Purif. Technol. 81 (2011) 88–93. https://doi.org/10.1016/j.seppur.2011.07.007.

[7] L.-S. Unger, R. Ruhl, M. Meffert, C. Niedrig, W. Menesklou, S.F. Wagner, D. Gerthsen, H.J.M. Bouwmeester, E. Ivers-Tiffée, Yttrium doping of Ba0.5Sr0.5Co0.8Fe0.2O3-δ part II: Influence on oxygen transport and phase stability, J. Eur. Ceram. Soc. 38 (2018) 2388–2395. https://doi.org/10.1016/j.jeurceramsoc.2017.12.042.

[8] M.P. Popov, I.A. Starkov, S.F. Bychkov, A.P. Nemudry, Improvement of Ba0.5Sr0.5Co0.8Fe0.2O3−δ functional properties by partial substitution of cobalt with tungsten, J. Membr. Sci. 469 (2014) 88–94. https://doi.org/10.1016/j.memsci.2014.06.022.

[9] E.V. Shubnikova, O.A. Bragina, A.P. Nemudry, Mixed conducting molybdenum doped BSCF materials, J. Ind. Eng. Chem. 59 (2018) 242–250. https://doi.org/10.1016/j.jiec.2017.10.029.

[10] S.K. Jaiswal, J. Kumar, Oxygen permeation characteristics of sol-gel derived barium-substituted strontium ferrite membranes, J. Am. Ceram. Soc. 100 (2017) 1306–1312. https://doi.org/10.1111/jace.14632.

[11] Y. Teraoka, H. Shimokawa, Ch.Y. Kang, H. Kusaba, K. Sasaki, Fe-based perovskite-type oxides as excellent oxygen-permeable and reduction-tolerant materials, Solid State Ion. 177 (2006) 2245–2248. https://doi.org/10.1016/j.ssi.2006.05.037.

[12] T. Klande, O. Ravkina, A. Feldhoff, Effect of microstructure on oxygen permeation of Ba0.5Sr0.5Co0.8Fe0.2O3−δ and SrCo0.8Fe0.2O3−δ membranes, J. Eur. Ceram. Soc. 33 (2013) 1129–1136. https://doi.org/10.1016/j.jeurceramsoc.2012.11.023.

[13] A. Berenov, A. Atkinson, J. Kilner, M. Ananyev, V. Eremin, N. Porotnikova, A. Farlenkov, E. Kurumchin, H.J.M. Bouwmeester, E. Bucher, W. Sitte, Oxygen tracer diffusion and surface exchange kinetics in Ba0.5Sr0.5Co0.8Fe0.2O3−δ, Solid State Ion. 268 (2014) 102–109. https://doi.org/10.1016/j.ssi.2014.09.031.

[14] P.-M. Geffroy, A. Vivet, J. Fouletier, M.C. Steil, E. Blond, N. Richet, P. Del Gallo, T. Chartier, The Impact of Experimental Factors on Oxygen Semi-Permeation Measurements, J. Electrochem. Soc. 160 (2013) F60–F68. https://doi.org/10.1149/2.068301jes.

[15] P.-M. Geffroy, E. Blond, N. Richet, T. Chartier, Understanding and identifying the oxygen transport mechanisms through a mixed-conductor membrane, Chem. Eng. Sci. 162 (2017) 245–261. https://doi.org/10.1016/j.ces.2017.01.006.

[16] M. Reichmann, P.-M. Geffroy, J. Fouletier, N. Richet, T. Chartier, Effect of cation substitution in the A site on the oxygen semi-permeation flux in La0.5A0.5Fe0.7Ga0.3O3−δ and La0.5A0.5Fe0.7Co0.3O3−δ dense perovskite membranes with A = Ca, Sr and Ba (part I), J. Power Sources. 261 (2014) 175–183. https://doi.org/10.1016/j.jpowsour.2014.03.074.

[17] X. Zhu, H. Wang, W. Yang, Structural stability and oxygen permeability of cerium lightly doped BaFeO3−δ ceramic membranes, Solid State Ion. 177 (2006) 2917–2921. https://doi.org/10.1016/j.ssi.2006.08.027.

[18] S.K. Jaiswal, J. Kumar, Structural and optical absorption studies of barium substituted strontium ferrite powder, Solid State Sci. 14 (2012) 1157–1168. https://doi.org/10.1016/j.solidstatesciences.2012.05.011.

[19] S. McIntosh, J.F. Vente, W.G. Haije, D.H.A. Blank, H.J.M. Bouwmeester, Structure and oxygen stoichiometry of SrCo0.8Fe0.2O3−δ and Ba0.5Sr0.5Co0.8Fe0.2O3−δ, Solid State Ion. 177 (2006) 1737–1742. https://doi.org/10.1016/j.ssi.2006.03.041.

[20] H. Wang, C. Tablet, A. Feldhoff, J. Caro, Investigation of phase structure, sintering, and permeability of perovskite-type Ba0.5Sr0.5Co0.8Fe0.2O3−δ membranes, J. Membr. Sci. 262 (2005) 20–26. https://doi.org/10.1016/j.memsci.2005.03.046.

[21] J.F. Vente, S. McIntosh, W.G. Haije, H.J.M. Bouwmeester, Properties and performance of BaxSr1−xCo0.8Fe0.2O3−δ materials for oxygen transport membranes, J. Solid State Electrochem. 10 (2006) 581–588. https://doi.org/10.1007/s10008-006-0130-2.

[22] B. Koo, K. Kim, J.K. Kim, H. Kwon, J.W. Han, W. Jung, Sr Segregation in Perovskite Oxides: Why It Happens and How It Exists, Joule. 2 (2018) 1476–1499. https://doi.org/10.1016/j.joule.2018.07.016.

[23] M. Reichmann, P.-M. Geffroy, N. Richet, T. Chartier, Impact of microstructure on oxygen semi-permeation performance of perovskite membranes: Understanding of oxygen transport mechanisms, J. Power Sources. 324 (2016) 774–779. https://doi.org/10.1016/j.jpowsour.2016.06.009.

[24] M. Arnold, J. Martynczuk, K. Efimov, H. Wang, A. Feldhoff, Grain boundaries as barrier for oxygen transport in perovskite-type membranes, J. Membr. Sci. 316 (2008) 137–144. https://doi.org/10.1016/j.memsci.2007.10.002.

[25] M. Reichmann, Développement de membranes céramiques à architecture optimisée pour l'oxycombustion, thesis, Limoges, 2014. http://www.theses.fr/2014LIMO0029 (accessed September 11, 2019).

[26] M. Mogensen, D. Lybye, N. Bonanos, P.V. Hendriksen, F.W. Poulsen, Factors controlling the oxide ion conductivity of fluorite and perovskite structured oxides, Solid State Ion. 174 (2004) 279–286. https://doi.org/10.1016/j.ssi.2004.07.036.

[27] P.-M. Geffroy, M. Reichmann, T. Chartier, J.-M. Bassat, J.-C. Grenier, Evaluating oxygen diffusion, surface exchange and oxygen semi-permeation in $Ln_2NiO_{4+\delta}$ membranes (Ln=La, Pr and Nd), J. Membr. Sci. 451 (2014) 234–242. https://doi.org/10.1016/j.memsci.2013.08.035.

[28] Z. Shao, W. Yang, Y. Cong, H. Dong, J. Tong, G. Xiong, Investigation of the permeation behavior and stability of a $Ba_{0.5}Sr_{0.5}Co_{0.8}Fe_{0.2}O_{3-\delta}$ oxygen membrane, J. Membr. Sci. 172 (2000) 177–188. https://doi.org/10.1016/S0376-7388(00)00337-9.

Figure captions

Table captions